

A-Site Cation Effect on Growth Thermodynamics and Photoconductive Properties in Ultrapure Lead Iodine Perovskite Monocrystalline Wires

Ligang Wang,^{†,‡} Yuan Huang,[‡] Aashir Waleed,[§] Ke Wu,[†] Cong Lin,[†] Zhengxu Wang,^{†,‡} Guanhaojie Zheng,[‡] Zhiyong Fan,[§] Junliang Sun,[†] Huanping Zhou,^{*,‡} Ling-Dong Sun,^{*,†} and Chun-Hua Yan[†]

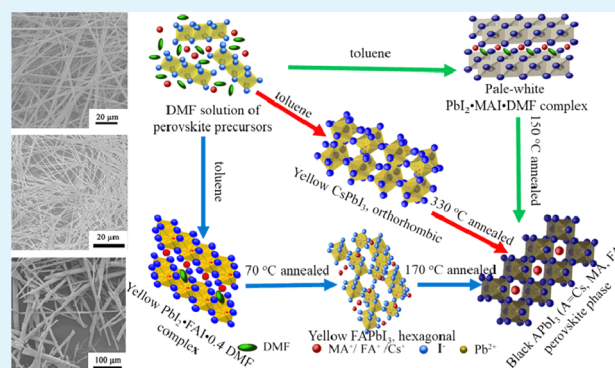
[†]Beijing National Laboratory for Molecular Sciences, State Key Laboratory of Rare Earth Materials Chemistry and Applications, PKU-HKU Joint Laboratory in Rare Earth Materials and Bioinorganic Chemistry, College of Chemistry and Molecular Engineering and [‡]Department of Materials Science and Engineering, Peking University, Beijing 100871, P. R. China

[§]Department of Electronic and Computer Engineering, The Hong Kong University of Science and Technology, Clear Water Bay, Kowloon, Hong Kong SAR 999077, P. R. China

Supporting Information

ABSTRACT: Among the various building blocks beyond polycrystalline thin films, perovskite wires have attracted extensive attention for potential applications including nanolasers, waveguides, field-effect transistors, and more. In this work, millimeter-scale lead iodine-based perovskite wires employing various A-site substitutions, namely, Cs, methylammonium (MA), and formamidinium (FA), have been synthesized via a new type solution method with nearly 100% yield. All of the three millimeter scale perovskite wires (MPWs) compositions exhibit relatively high quality, and CsPbI₃ is proven to be monocrystalline along its entire length. Furthermore, the growth thermodynamics of the APbI₃ MPWs with respect to A-site cation effect were studied thoroughly by various characterization techniques. Finally, single MPW photodetectors have been fabricated utilizing the APbI₃ MPWs for studying the photoconductive properties, which show different sensitivities under illumination. This systematic synthesis method of solution-processed APbI₃ (Cs, MA, and FA) MPWs reveals a wide spectrum of additives with different coordination capability that mediates perovskite materials growth. It proved to serve as a new parameter that further aids in the rational process of the polycrystalline organic/inorganic hybrids materials. These MPWs also have the potential to open up new opportunities for integrated nanoelectronics ranging from the nanometer through millimeter length scales.

KEYWORDS: perovskite, photodetector, monocrystalline, thermodynamics, wire



INTRODUCTION

Organic–inorganic hybrid perovskites have attracted tremendous research efforts in recent years due to their unique optical and electronic properties. The extremely low fabrication costs and rapid advancement in power conversion efficiency from 3.8% to a certified 22.1%^{1–6} in merely couple of years makes hybrid perovskite solar cell a promising and competitive photovoltaic technology. In addition to photovoltaic, its exquisite optoelectronic properties, such as low recombination rates, long diffusion lengths, and a high defect tolerance, render perovskites attractive materials for other technologies⁷ such as field effect transistors,^{8–11} light-emitting diodes,^{10–12} lasers, and photodetectors.^{13,14} Recent progress in perovskite-based optoelectronic devices has been realized by a delicate control of materials growth, as well as a deep understanding of the

fundamental material properties and operational mechanisms of the devices. However, exploration of the different forms of perovskite semiconductors beyond the widely used polycrystalline thin films is crucial to further exploit their exceptional properties and realize the applications arising from nanostructured and macroscopic single crystals.

Due to the appeal of the high aspect ratio of one-dimensional (1D) materials, perovskite wires pose additional attractions that differ from the zero-dimensional nanocrystals,¹⁵ two-dimensional nanosheets,¹⁶ and three-dimensional single crystals.¹⁷ One of the most attractive applications for perovskite wires is a

Received: May 1, 2017

Accepted: July 13, 2017

Published: July 13, 2017

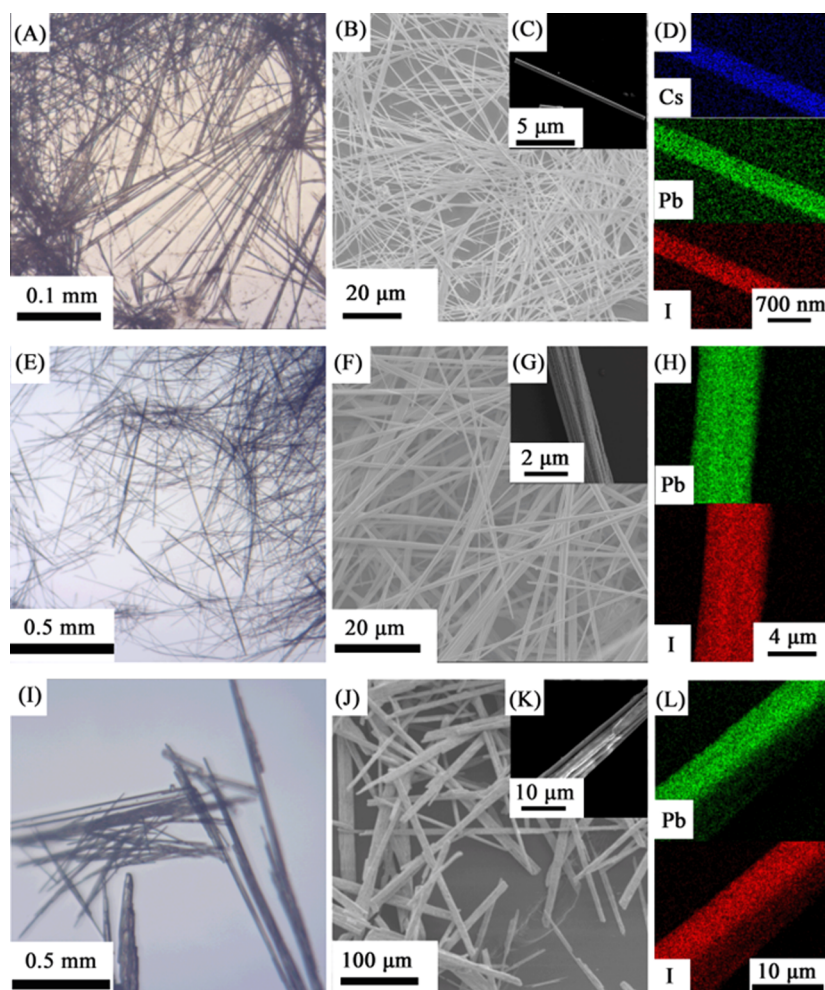


Figure 1. Optical and SEM images of MPWs without the thermal treatment: (A) optical image; (B) SEM image; (C) high-resolution SEM image; (D) elemental mapping of CsPbI₃ MPWs; (E–H) images of MAPbI₃ MPWs; (I–L) images of FAPbI₃ MPWs correspondingly.

miniaturized laser,^{18–21} which is a result of the improved carrier diffusion along the wires. In fact, Jin et al.²² have demonstrated lead halide perovskite wires lasers with low lasing thresholds and high quality factors. Furthermore, they identified morphological effects on carrier diffusion and the laser mode, with a Fabry–Pérot cavity in the wires^{23–25} and a whispering gallery mode in nanoplates.^{26–28} Other unique characteristics of perovskite wires, such as high charge carrier mobility and broad tunable absorption bands, enable their expansion to photodetector applications. Photodetectors that detect light by converting optical signals into electrical current find numerous applications in light detection,²⁹ optical communication,³⁰ imaging,³¹ and so on. Earlier studies have demonstrated that perovskite-based detectors yield high sensitivity, detectivity, speeds, and a broad spectral photoresponse.³² As of now, the majority of perovskite photodetectors have been based on perovskite single crystals and polycrystalline films,³³ whereas miniaturized photodetectors based on wires have rarely been reported. The potential application of perovskite materials in miniaturized optoelectronic devices, such as microcircuits, miniaturized sensors, trace detection, and so on, highlights the importance of developing systematic synthesis methods and establishing a fundamental understanding of the composition–property relationships of the perovskite wires.

In an attempt to obtain perovskite wires, a variety of synthetic methods have been studied that include two-step

solution immersion,¹⁹ thermolysis,³⁴ and chemical vapor deposition.³⁵ However, research efforts based on these methods are limited to the synthesis of one or two types of perovskite wires (e.g., MAPbI₃ wires) rather than widely applicable to a range of perovskite compositions. A-site substitution in ABX₃ perovskite materials is crucial to create perovskites with distinct properties due to the altered crystal structure and electronic configuration.^{36,37} The research efforts to understand the A-site cation effect in perovskite materials were mainly subjected to polycrystalline film and nanocrystals, and identified different phase/thermal stability, optoelectronic property, and photostability.^{38–42} Very recently, mixed A-site cation perovskite film was found in single-junction and multijunction solar cells due to the substantially improved stability and device performance compared with that of its counterpart.^{43,44} Additionally, mixed Cs/formamidinium (FA) nanocrystals were proven to exhibit a ultrahigh photoluminescence (PL) quantum efficiency and a perfect stability.⁴⁵ With respect to low-dimensional perovskite wires, there is no report that systematically studied the A-site effect in ABX₃ perovskite wires in the context of both growth thermodynamics and photoelectric properties.

In this work, a new type of solvent-mediated method was developed for preparing highly uniform and millimeter-scale APbI₃ (A = methylammonium (MA), FA, and Cs) perovskite wires (MPWs). The synthesis of ultralong MPWs involves the formation of Pb-complex clusters in *N,N*-dimethyl formamide

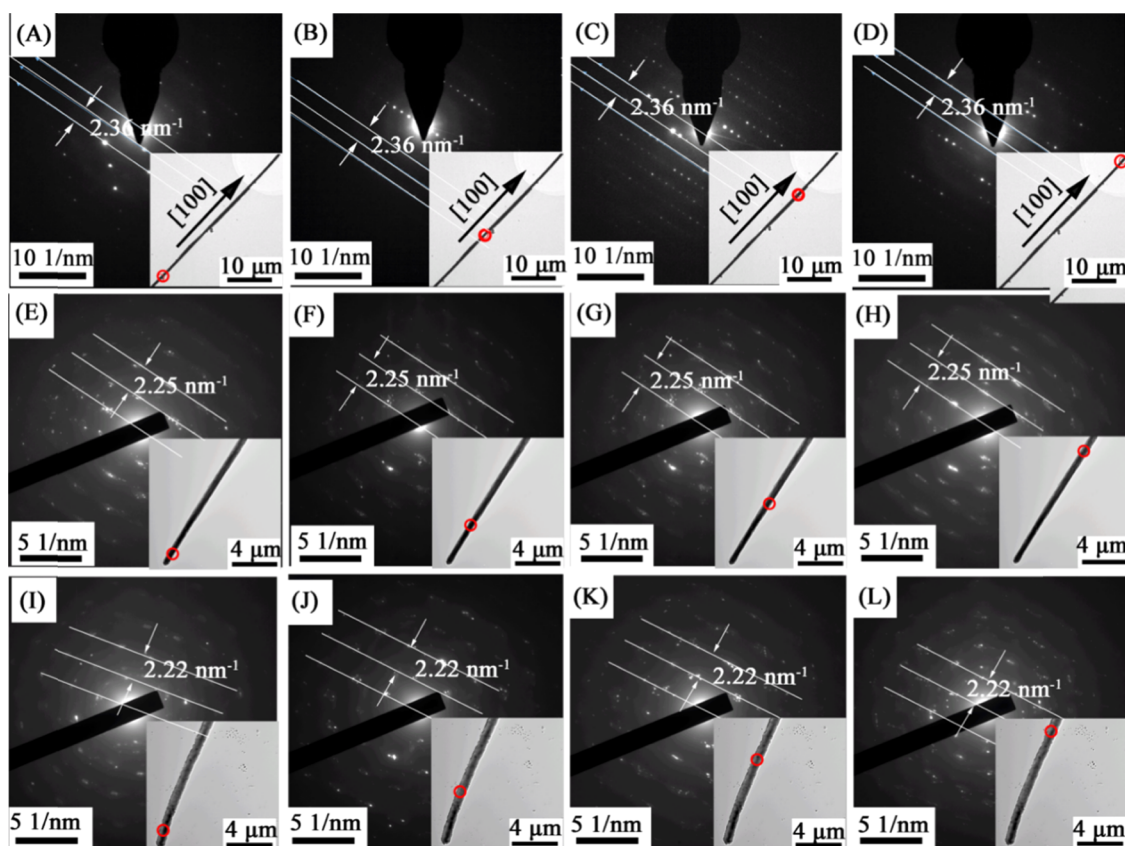


Figure 2. SAED patterns of MPWs. (A–D) CsPbI₃ MPWs without heat treatment; (E–H) MAPbI₃ MPWs with heat treatment; (I–L) FAPbI₃ MPWs with heat treatment. Red circle in the inserted graph indicates the position on MPWs where SAED was performed.

(DMF), followed by intermediate MPWs phase induced by antisolvent exposure, and finally the MPW formed via proper thermal treatment. Accordingly, we have successfully synthesized CsPbI₃, MAPbI₃, and FAPbI₃ MPWs of millimeter-scale lengths with a nearly 100% yield. Interestingly, the typical CsPbI₃ MPWs were all found to be single crystals along the entire wire. The growth process of APbI₃ MPWs was monitored via a combination of X-ray diffraction (XRD), transmission electron microscopy (TEM), thermogravimetric analysis (TGA), dynamic light scattering (DLS), and differential scanning calorimetry (DSC), and so on. We further studied the growth mechanisms of the APbI₃ MPWs formation by observing the halide effects. The growth process of APbI₃ MPWs is substantially different along the A-site substitution. Photodetectors based on a single APbI₃ (A = MA or FA) MPW showed a good but distinct photoresponse. We elaborately studied and revealed the differences in the growth mechanism and thermal, optical, and photoconductive properties of APbI₃ with substitutions, which could serve as a new parameter for organic/inorganic hybrid perovskite polycrystalline and nanomaterials design. These uniform ultralong MPWs may also serve as an ideal model to study high-performance semiconductor nanodevices and obtain a fundamental understanding of low-dimensional material properties.

RESULTS AND DISCUSSION

MPWs Synthesis and Morphology Characterization.

APbI₃ (A = Cs, MA, and FA) MPWs were synthesized by a solvent-mediated growth method. In a typical synthesis, the precursors (AI, PbI₂) with a given stoichiometric ratio were

added into a DMF solvent and stirred for 1 h at 70 °C. The precursor solutions were then cooled to room temperature, followed by the introduction of a certain amount of toluene into the solution. The precipitation of ultralong intermediate/interphase MPWs was obtained via centrifugation, and these intermediate phases were further transformed into the final MPWs after the thermal treatment (330 °C for CsPbI₃, 150 °C for MAPbI₃, and 170 °C for FAPbI₃). The morphology and composition of lead iodide MPWs was characterized by optical microscopy, scanning electron microscopy (SEM), and energy dispersive X-ray spectroscopy (EDS). Figure 1A,E,I shows the images of MPWs under an optical microscope, indicating the highly uniform and ultralong features of the as-formed MPWs. Surprisingly, the yield of the MPWs is nearly 100%, without any coexisting nanoparticles. Almost all of the MPWs are straight with a narrow diameter distribution. SEM and enlarged SEM images in Figure 1 provide further information regarding the dimensions of these MPWs. It is quite interesting that the lengths of all of the APbI₃ (Cs, MA, and FA) MPWs reached a millimeter-scale length (Figure 1A,E,I); however, the diameters of the MPWs varied dramatically (Figure 1C,G,K). We found that the diameters for CsPbI₃ MPWs were the smallest (nearly 300 nm), whereas that of FAPbI₃ wires were the largest (0.8–6 μm), and that of MAPbI₃ wires (0.5–2 μm) was in between. The dependence of the APbI₃ diameter on the A-site cation will be discussed later in the mechanism section. Next, the EDS was used to investigate the composition of the APbI₃ MPWs. The results (Figure S1) demonstrate that the average atomic ratio of Cs/Pb/I in CsPbI₃ MPWs was 0.18:0.22:0.60, which is in accordance with the stoichiometric ratio of the CsPbI₃ (1:1:3) solution, taking the associated error of EDS into consideration.

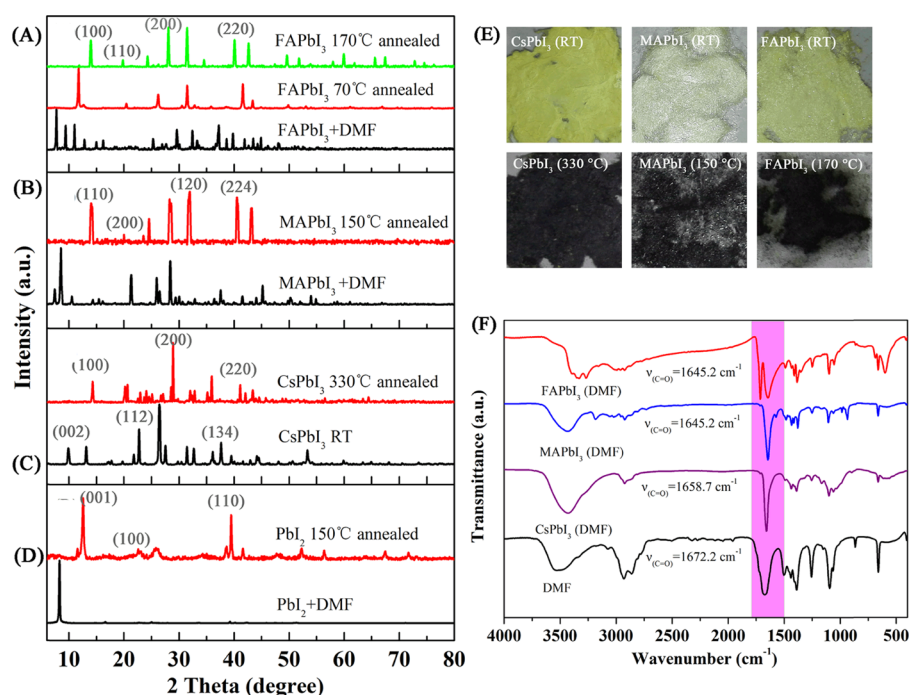


Figure 3. XRD, Fourier transform infrared (FTIR) characterization, and the corresponding color changes of the APbI₃ (Cs, MA, and FA) MPWs before and after thermal treatment. XRD of MPWs before and after 10 min thermal treatments at the specified temperatures for (A) FAPbI₃; (B) MAPbI₃; (C) CsPbI₃. (D) XRD of PbI₂ + DMF complex prepared under same conditions for comparison. (E) Color changes of APbI₃ MPWs before and after thermal treatment. (F) FTIR of APbI₃ before thermal treatment.

Similarly, the calculated ratios of Pb/I were 0.25:0.75 for MAPbI₃ MPWs and 0.27:0.73 for FAPbI₃ MPWs. This is in excellent agreement with the stoichiometric ratio (1:3) of Pb/I in the APbI₃ precursor. The elemental mapping of the APbI₃ MPWs further confirmed that the elemental distribution, such as Cs, Pb, and I in CsPbI₃ and Pb and I in MAPbI₃ and FAPbI₃, was uniform. The absence of the MA signal in MAPbI₃ and the FA signal in FAPbI₃ is ascribed to their low molecular weight. TEM and selected area electron diffraction (SAED) were further utilized to characterize the as-obtained MPWs. Amazingly, the typical CsPbI₃ MPWs were proven to be monocrystalline along the entire wire and the MAPbI₃ and FAPbI₃ MPWs possess a continuous and coherent orientation along the entire wire. Figure 2A–D depicts the SAED analysis of typical CsPbI₃ MPWs on an area with a probe diameter of approximately 300 nm. The pattern reveals the diffraction characteristics of a single crystal. To prove the entire MPWs are monocrystalline, SAED was performed on multiple positions along the entire CsPbI₃ MPWs, as shown in Figure 2A–D. The diffraction patterns of four different positions, from head to tail, all appeared as single distributed spots with identical orientation and the measured reciprocal spacing was 2.36 nm⁻¹, which confirms the single-crystal nature and consistent orientation of the entire MPWs. MPWs, especially MAPbI₃ and FAPbI₃, are fragile under electron of high-resolution TEM, so it is difficult to get the lattice fringe images to recognize the orientation directly.

We further examined the preferred orientation of MPWs by means of the XRD coupled with March–Dollase simulation. The XRD characterization of MPWs with different treatments (with or without grinding) was performed under both reflection and transmission modes. The sample without the grinding exhibited obvious orientation under the reflection mode; however, most of them diminished after a fine grinding.

Furthermore, most of the orientation could be eliminated completely under the transmission mode. As shown in Figure S2A,B, the relative peak intensity changed obviously, which announced the existence of orientation. Because of the extinction rule of diffraction, some low-index facet that reveal the orientation could not be observed. March–Dollase simulation method is utilized to calculate the XRD pattern of a low-index facet growth orientation (the crystal structure was downloaded from the existing report).⁴⁶ The pattern of 100 orientation accords well with the instrument result, which shows 100 as the possible growth orientation. SAED is another strong method to identify the orientation. As shown in Figure S2C,D, the *d*-spacing of the simulated SAED patterns 0.890, 0.463, and 0.240 nm accorded well with the measured results, which correspond to (002), (101), and (200) planes. The simulated and measured result affirm that 100 is the preferred orientation. MAPbI₃ and FAPbI₃ MPWs were also studied in a similar method, and both of them demonstrated crystalline characteristics (Figure 2E–L). The diffraction patterns of MAPbI₃ and FAPbI₃ MPWs showed an analogous spot distribution. The reciprocal spacing of MAPbI₃ and FAPbI₃ was 2.25 and 2.22 nm⁻¹, respectively, but the conspicuous satellite spot could be observed, this may be induced by an inherent defect and a high-power electron beam. The same method was used to identify the orientation of MAPbI₃ and FAPbI₃ MPWs (Figures S3A,B and S4A–C). The result showed that the orientation was probably 001 and 100, respectively. To the best of our knowledge, this was the first time that monocrystalline MPWs have been confirmed.

Intermediate Phase Confirmation. To identify the presence of intermediate phases during MPWs growth, the XRD measurements were conducted before and after the thermal treatment. Figure 3A–D depicts the XRD patterns of the APbI₃ MPWs before and after the thermal treatment. It was

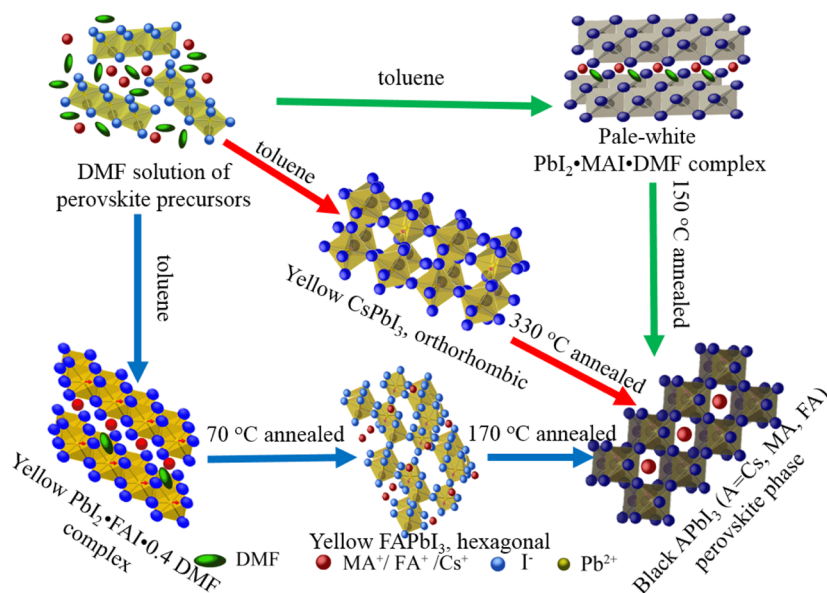


Figure 4. Schematic of APbI₃ MPWs growth mechanism.

found that CsPbI₃ MPWs with an orthorhombic phase was formed at room temperature without any additional thermal treatment. The phase formation at room temperature suggested a relatively low formation energy for CsPbI₃, which was consistent with previous reports.⁴⁷ After the thermal treatment at 330 °C, CsPbI₃ MPWs underwent a phase transition in their cubic phase, accompanied by a color change from the original yellow to black. The MPWs exhibited a phase change from orthorhombic to cubic at 330 °C, similar to the polycrystalline films, indicating the CsPbI₃ phase transformation is independent of morphology/geometry. TGA (Figure S5A) conducted for CsPbI₃ MPWs showed that the sample lost 63.3% of its weight before reaching 70 °C, which likely corresponds to the removal of adsorbed solvents such as toluene and weakly bound DMF. Moreover, CsPbI₃ sample began to sublimate at 470 °C and was fully volatilized at a temperature of 600 °C. DSC measurements indicated that a strong negative heat flow occurred at 322.1 °C, which could be ascribed to the suggested phase transformation from orthorhombic to cubic.

The growth process for MAPbI₃ and FAPbI₃ MPWs are quite different from that for CsPbI₃. As shown in Figure 3F, without the thermal treatment, both MA- and FA-based MPWs possess several distinctive peaks at low 2θ angles of 7.4, 8.5, and 10.5° for the MAPbI₃ system and 7.7, 9.4, and 11.0° for the FAPbI₃ system. These low angle peaks can be assigned to a PbI₂ complex, where the cation (MA⁺ or FA⁺) and/or the solvent (DMF) is inserted into the PbI₂ framework, as the diffraction pattern shifted to a lower angle when compared with PbI₂. This is an indication of the lattice expansion induced by the cations or solvent-induced PbI₂ complexes. The room temperature “product” is hereinafter referred to as an “intermediate”. After both MA- and FA-based materials were further annealed, the low angle peaks disappeared from the XRD pattern. The MA-based products after 150 °C annealing exhibited a set of strong peaks located at 14.1, 31.9, and 40.7°, corresponding to a tetragonal MAPbI₃. Similarly, the FA-based products after 170 °C treatment also displayed strong peaks located at 13.9, 31.5, and 40.2°, which correspond to a cubic FAPbI₃. This suggests that the intermediate decomposed and the resulting perovskite phase was formed. This was also reflected by the color change

from that of the intermediate to the desired crystal phase. MAPbI₃ turned from a pale-white at room temperature to black at 150 °C, whereas FAPbI₃ changed from yellow at room temperature to black at 170 °C. TGA was used to further assist in showing the formation of PbI₂–methylammonium iodide (MAI)–DMF and PbI₂–formamidinium iodide (FAI)–DMF intermediates during MPWs growth (Figure S5B,C). For the MA-based MPWs, a 53.7% weight loss was observed before 45 °C, which may be ascribed to toluene and weakly bound (or unbound) DMF molecules. Furthermore, a 5.5% weight loss between 45 and 70 °C was observed, which may correspond to a strongly bonded DMF; a 10.2% weight loss between 250 and 300 °C, likely due to MAI volatilization; and finally a 33.4% loss at 400 °C, which suggests that the residual PbI₂ sublimated. On the basis of this analysis, it can be deduced that the composition of this intermediate is MAI/PbI₂/DMF (1:1:1). The FAPbI₃ system showed similar results to those of MAPbI₃, suggesting an intermediate composition of FAI/PbI₂/DMF (1:1:0.4) based on the TGA results (Figure S5C). The DSC measurements of MA-based products (Figure S6B) showed a strong endothermic peak at 107 °C, which may correspond to the formation of the MAPbI₃ phase. When the temperature reached 120 °C, the two additional peak shoulders appeared, potentially indicating a further phase change from tetragonal to cubic. In contrast, a sharp endothermic peak at 143.4 °C (Figure S6C) was observed in the FA-based system, confirming the phase change from hexagonal to cubic.

FTIR spectroscopy was used to further examine the bonding nature between DMF and the precursor materials, as shown in Figure 3F. Interestingly, the CsI–PbI₂ precursor exhibited quite different interactions with DMF compared with the MAI–PbI₂ and FAI–PbI₂ precursors. In CsI–PbI₂, a vibrational stretching C=O peak shifted slightly from 1672.2 cm⁻¹ (pure DMF solvent) to 1658.7 cm⁻¹. The coordination capability between DMF and MAI–PbI₂/FAI–PbI₂ precursors existed similarly, as evident by the C=O peak shift from 1672.2 to 1645.2 cm⁻¹. As a larger shift of C=O vibration suggested a stronger coordination between C=O and the precursors, this indicated that the coordination between DMF and the CsI–PbI₂

precursor is weaker than that between the MAI–PbI₂ and FAI–PbI₂ precursors.

In contrast, PbI₂ was also used as a single precursor source to fabricate wires via the same method. It is quite interesting that the solvent intercalation could enable PbI₂ MPWs formation. However, the diameters were larger than 10 μm, which was different from the APbI₃ series, as shown in the SEM images (Figure S7). The corresponding XRD analysis is provided in Figure 3D, where the as-formed rods exhibit a strong peak at 8.3°, indicative of a PbI₂ complex. After thermal treatment, the diffraction peak from the PbI₂ complex disappeared completely, and the peaks from the hexagonal phase of PbI₂ emerged. This further suggested that the formation of MPWs may rely on the intermediate, and the diameter of the final MPWs can be varied dramatically by the precursors, which will be discussed in the following section.

On the basis of the above characterization, we proposed a possible growth mechanism for APbI₃ MPWs (Figure 4). The Cs, MA, and FA systems underwent different growth process. In the MA- and FA-based systems, ultralong MPWs consisting of MAI–PbI₂–DMF or FAI–PbI₂–DMF intermediates, respectively, were formed upon the introduction of toluene antisolvent. A yellow hexagonal FAPbI₃ intermediate phase was proven to exist via proper heat treatment (70 °C) under vacuum and transformed into black perovskite after heating at 170 °C. However, no stable intermediate phase was observed for the MAPbI₃ MPWs, as the black perovskite phase emerged from the treatment at 150 °C. The growth process for CsPbI₃ was an entirely different story. A CsI–PbI₂–DMF intermediate was not observed, but a stable interphase was formed, followed by a phase transformation from a yellow orthorhombic to black cubic phase under an even higher temperature treatment.

The origin of the above difference in the growth processes and the roles of DMF and toluene are suggested in the following proposed mechanism: due to chelation effects, the DMF molecules and cations intercalate into the PbI₂ sheetlike framework while in their respective precursors solution. The chelated DMF gradually enlarges the distances between the framework, resulting in a dimension reduction from bulk PbI₂ into dispersed sheetlike pieces. This is characteristic of a colloidal solution, as proven by the DLS measurements provided in Figure S8. After the introduction of the toluene antisolvent, the chelated DMF is then forced out from the layered framework, inducing the formation of the MPWs structure. The combination of chelated DMF and toluene herein plays a vital role in initiating the assembly process for the formation of MPWs. The amount of toluene required is different for each material system. For instance, CsPbI₃ is readily formed without an intermediate formation, which means that a small amount of toluene is needed to extract the subtle amount of chelated DMF. This could potentially be ascribed to the small radius and more rigid perovskite framework resulting from Cs⁺ that enables a more compact crystal lattice and a weaker intermolecular interactions between DMF and CsI. However, to form MAPbI₃ and FAPbI₃ MPWs, more toluene is required due to the increased amount of chelated DMF within the intermediate. The formation differences between CsPbI₃ and MAPbI₃/FAPbI₃ MPWs can be explained via the following: (1) the radius of MA⁺ and FA⁺ are larger than that of Cs⁺, which enables more open crystal lattices for MAPbI₃/FAPbI₃ than for CsPbI₃; (2) DMF can interact with MAI/FAI in the form of hydrogen bonding or dipolar interaction, facilitating the formation of stable MAI–PbI₂–DMF/FAI–PbI₂–DMF inter-

mediates. Regardless of the existence of an intermediate phase, the intercalation of DMF into the PbI₂ framework can alter the energetics within different crystal planes. Most likely, the more favorable crystal growth direction is in-line with the PbI₂ sheet plane, which promotes the formation of ultralong MPWs.

In addition to APbI₃, chlorine- and bromine-based perovskites (APbX₃, A = Cs, MA, and FA; X = Cl and Br) were studied under identical synthetic conditions. It was found that in most material systems, a large degree of precipitation resulted from toluene addition into the precursor solution (Figure S9A–I). The SEM characterizations (Figure S10A–F) of these precipitations showed the presence of microscale particles instead of ultralong MPWs. Figure S11A,B displays the XRD patterns of the precipitations before and after thermal treatment. Accordingly, chlorine-based precipitation shows the coexistence of APbCl₃ and PbCl₂, without the Pb complex, whose peak is located at a low angle (<10°). This suggests that the intermediate ACl–PbCl₂–DMF did not form under these circumstances. Similarly, bromine-based precipitation does not show the existence of an ABr–PbBr₂–DMF intermediate. The absence of an intermediate in the chlorine and bromine perovskite systems could be the reason they do not form 1D structures, which further highlights the importance of the intermediates for achieving ultralong MPWs.

We ascribed the above growth differences mainly to the different crystal structure/crystal lattice energies of PbX₂ and the interaction between PbX₂/DMF. Regarding the crystal structure, both PbCl₂ and PbBr₂ are orthorhombic, whereas PbI₂ is hexagonal with a lamellar packing. This lamellar packing feature in PbI₂ may facilitate the formation of low-dimensional structures. In addition, the crystal lattice energies of PbX₂ and the interactions between PbX₂/DMF simultaneously determine the presence of chelated DMF inside the PbX₂ framework. The crystal lattice energy of PbX₂ decreases in sequence PbCl₂ (2270 kJ/mol) to PbBr₂ (2219 kJ/mol) to PbI₂ (2163 kJ/mol). Additionally, the coordination capability of DMF toward PbX₂ increases in the order of PbCl₂ → PbBr₂ → PbI₂ due to the softer nature of PbI₂. Therefore, the solubility of PbX₂ in DMF increases from Cl → Br → I, where PbCl₂ has a very limited solubility and PbI₂ can be easily dissolved (reach 35% wt).⁴⁸ The low solubility of PbCl₂ and PbBr₂ in DMF resulted in decreased interactions with DMF, leading to the absence of ultralong intermediate formation during the growth process. Herein, we frequently observed the coexistence of the lead halide and the corresponding perovskite phases (PbCl₂/APbCl₃, PbBr₂/APbBr₃).⁴⁹ In addition, the structural differences between the above perovskites could serve as another possible explanation. Table S1 and Figure S12 indicate that the tolerance factors (τ) of Br[−] and Cl[−] based perovskites are larger than those of the iodine-based perovskites. This results in a higher symmetry for Cl and Br than for iodine perovskites, which hindered the formation of ultralong structures.

To further investigate the mechanism of MPWs formation, additional I[−] was intentionally introduced into the precursor solution. For example, hydrogen iodide (HI) was introduced into the CsI–PbI₂ precursor solution containing DMF solvent. As shown in Figure S13, when the molar ratio of extra I[−] from HI is equivalent to that of I[−] in the original CsPbI₃, an ultralong MPWs would no longer form. Instead, sheetlike or square particles are formed. This may be related to the formation of H_{1−x}PbI_{3−x} induced by HI, as suggested by previous works.⁵⁰ As H_{1−x}PbI_{3−x} was well-dispersed, the PbI₂ framework could be

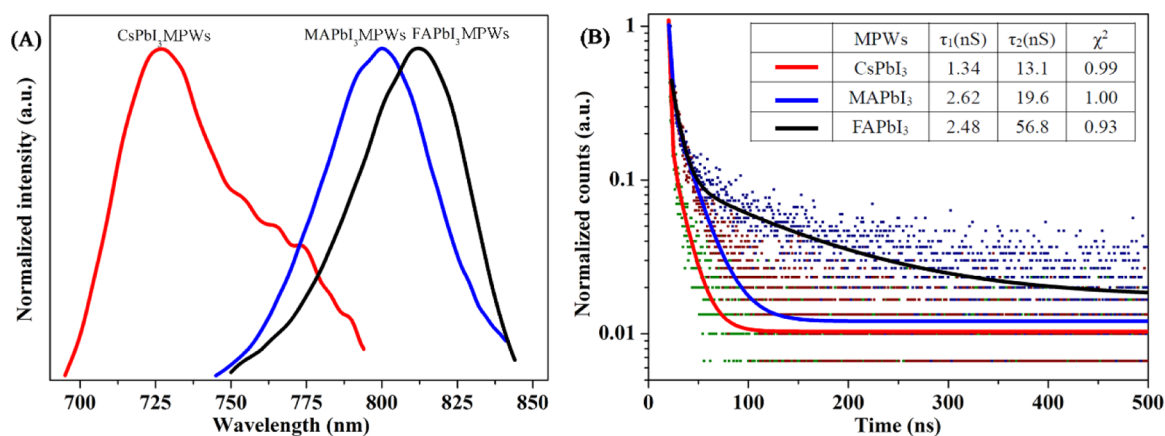


Figure 5. Fluorescence and lifetime characteristics of the APbI₃ MPWs on glass after thermal treatment. (A) PL of APbI₃ MPWs, wavelength of excitation light was 470 nm. (B) PL decay kinetics of APbI₃. Detected light wavelength was 727 nm for CsPbI₃ MPWs, 800 nm for MAPbI₃ MPWs, and 810 nm for FAPbI₃ MPWs. The decay dynamics was fitted by biexponential equation, and the inserted table was the fitting result.

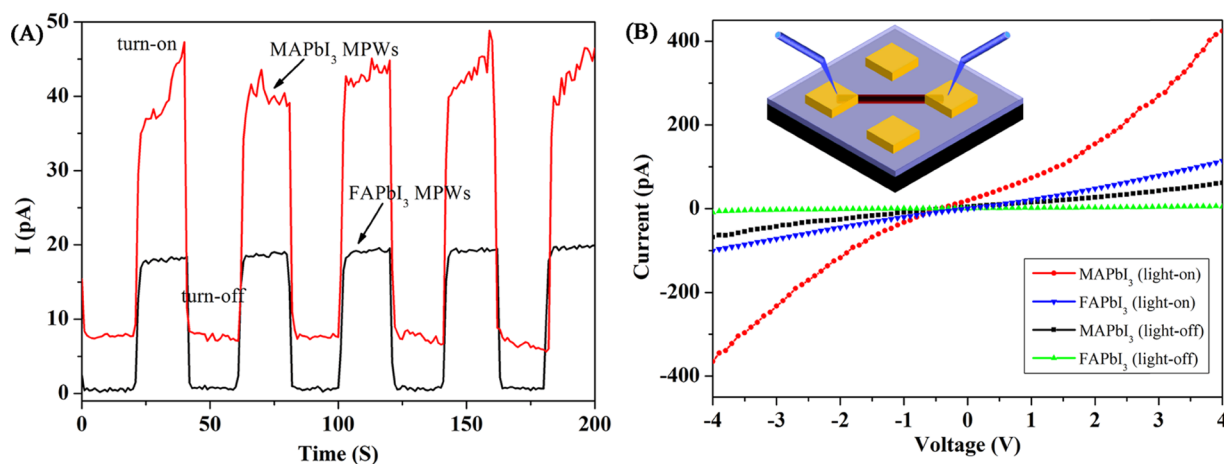


Figure 6. Photodetector based on a single perovskite wire. (A) Current–time curves of MAPbI₃ and FAPbI₃ MPW-based photodetectors at a bias voltage of 1 V. (B) Current–voltage curves of MAPbI₃ and FAPbI₃ MPW under dark and illuminated states. The insertion represents the structure of MPW photodetector.

easily destroyed, preventing the formation of ultralong structures during antisolvent introduction.

PL Characterization. To investigate the resulting optical properties of the APbI₃ MPWs, we performed PL measurements on MPWs dispersed onto glass slides after thermal treatment. As shown in Figure 5A, the emission peaks for CsPbI₃, MAPbI₃, and FAPbI₃ MPWs are 727, 80, and 812 nm, respectively. These emission peak shifts are in accordance with the respective band gaps: CsPbI₃ ($E_g = 1.74$ eV); MAPbI₃ ($E_g = 1.55$ eV); FAPbI₃ ($E_g = 1.50$ eV).⁵¹ Time-resolved PL experiments were performed upon 470 nm excitation and the APbI₃ MPWs samples were sealed in dry air to avoid phase destruction. The PL decay was fitted using a biexponential equation. As shown in Figure 5B, the fitted PL lifetimes are 1.44 and 16.44, 6.84 and 38.91, and 2.31 and 63.28 ns for CsPbI₃, MAPbI₃, and FAPbI₃, respectively. The two decay components could originate from a surface component (fast) and bulk component (slow). Apparently, the bulk decay time of these materials increased following the sequence CsPbI₃ → MAPbI₃ → FAPbI₃. Different decay constants for these three materials were a direct indication of different recombination rates within these MPWs, which likely related to intrinsic defects or those originating from fabrication processes. This suggests that FAPbI₃ MPWs likely possess a reduced defect

density among the APbI₃ series, which ought to benefit the corresponding optoelectronic device performance.

Single MPW-Based Photodetectors. Photoconductive properties of a single MPW were investigated based on photodetector fabrication. The single-MPW devices (Figure S14A–C) were prepared by using the following procedure. The MPWs were first dispersed in toluene by continuous sonication and stirring for 30 min, followed by dipping onto a 100 nm SiO₂-coated silicon wafer (1.5×1.5 cm²), and then heat treated in N₂ atmosphere at a proper temperature (150 °C for MAPbI₃, 170 °C for FAPbI₃, 330 °C for CsPbI₃). Finally, a 200-mesh TEM naked copper grid was used as the mask for the gold electrode evaporation. Current–voltage (C–V) and current–time (C–T) curves (Figure 6A,B) of the corresponding devices were obtained by using a Keithley 4200 equipped with a microprobe station and a tungsten lamp. A two-terminal measurement method was used at a bias voltage of 1 V. As shown in Figure 6A, both MAPbI₃ and FAPbI₃ MPWs showed good photoresponsivity, but the cubic CsPbI₃ MPWs failed to exhibit similar behaviors due to their extreme instability under the measurement conditions (Figure S15). Formation of Schottky junction between MAPbI₃/FAPbI₃ and the gold electrode could be confirmed by the current–voltage curve (Figure 6B). When illumination was on, the carrier density

increased obviously and effective barrier height decreased, which leads to faster carriers tunneling and transportation. The steeper current–voltage curve under illumination affirms the enhancement of conductivity. The current value of MAPbI₃/FAPbI₃ MPWs in the dark state (light off) and illuminated state (light on, 1.9 mW/cm²) showed apparent differences (Figure 6A). The average on/off ratio (S , define as $S = I_{\text{light}}/I_{\text{dark}}$) reached 5.3 for MAPbI₃ and 25.6 for FAPbI₃ MPWs. The responsivity (R) of a photodetector is defined as $R = \Delta I/(P \times A)$ ($\Delta I = I_{\text{light}} - I_{\text{dark}}$, P is the intensity of illumination light, A is the device area). The R of MAPbI₃ and FAPbI₃ photodetector reached 0.0428 and 0.0095 A/W, respectively. The rise time (T_r) and decay time (T_d) reflect the photoresponse speed, which was defined as the time take for the photocurrent ($I_{\text{ph}} = I_{\text{light}} - I_{\text{dark}}$) to increase from $0.1I_{\text{ph}}$ to $0.9I_{\text{ph}}$ or decrease from $0.9I_{\text{ph}}$ to $0.1I_{\text{ph}}$. As shown in Figure S16A,B, the rise time and decay time of MAPbI₃/FAPbI₃ single wire based photodetector were 1.5 and 1.0 s and 1.4 and 0.9 s, respectively. This performance was comparable with that of zinc octaethylporphyrin single nanowire-based photodetector ($T_r = 0.9$ s and $T_d = 1.7$ s)⁵² and Zn₃As₂ nanowire-array-based photodetector ($T_r = 0.14$ s and $T_d = 2.9$ s) under white light illumination.⁵³

CONCLUSIONS

In conclusion, millimeter-scale ultralong CsPbI₃, MAPbI₃, and FAPbI₃ series MPWs were synthesized by a simple solution-based method. The resulting MPWs are highly uniform, with a nearly 100% yield. SAED results show the monocrystalline nature of CsPbI₃ MPWs along the entire millimeter-scale wire. The formation process of ultralong MPWs involves the formation of DMF-complex intermediate, but the growth process of APbI₃ MPWs is different with the A-site substitution. In addition, photodetectors based on a single APbI₃ MPW were fabricated and exhibited good but different sensitivities to illumination, which can be utilized for use in microcircuits, optical imaging, photodetection, and more. We systematically studied the growth thermodynamics and photoconductive properties along substitutions. Furthermore, these ultrapure and high-quality MPWs also present an ideal model to study nanoscale semiconductor devices, such as nanolasers, waveguides, and so on, as well as the fundamental properties of 1D perovskite materials.

ASSOCIATED CONTENT

Supporting Information

The Supporting Information is available free of charge on the ACS Publications website at DOI: 10.1021/acsami.7b05875.

Materials and methods; EDS, simulated XRD, SAED, TGA, and DSC of APbI₃ MPWs; SEM images of PbI₂ rods, APbCl₃, APbBr₃ particles; DLS of APbI₃ precursor solution; tolerance factor distribution diagram; optical images of photodetectors; current–time curves; photocurrent rise and decay of single-wire photodetector; the calculation process of on/off ratio (S) and responsivity (R) (PDF)

AUTHOR INFORMATION

Corresponding Authors

*E-mail: happy_zhou@pku.edu.cn (H.Z.).

*E-mail: sun@pku.edu.cn (L.S.).

ORCID

Aashir Waleed: 0000-0002-6929-8373

Zhiyong Fan: 0000-0002-5397-0129

Huanping Zhou: 0000-0003-4220-1161

Chun-Hua Yan: 0000-0002-0581-2951

Notes

The authors declare no competing financial interest.

ACKNOWLEDGMENTS

This work was supported by NSFC (Nos. 21425101, 21321001, 21371011, 21331001, and 51672008); MOST of China (2014CB643800); and Young Talent Thousand Program. The authors sincerely thank Prof. Ming Li group from PKU and Prof. Zhiyong Fan group from Hong Kong University of Science and Technology for providing photodetector testing; Hubbard from University of California, Los Angeles, for helping in SAED analysis. The following groups made quite a lot attempts in fabricating MPWs lasers/waveguide are highly appreciated: Prof. Xingyuan Liu group from Chinese Academy of Sciences Changchun Optical Precision Machinery and the Institute of Physics, Prof. Shufeng Wang group from PKU and Prof. Xiaoyong Hu group from PKU.

REFERENCES

- (1) Kojima, A.; Teshima, K.; Shirai, Y.; Miyasaka, T. Organometal Halide Perovskites as Visible-Light Sensitizers for Photovoltaic Cells. *J. Am. Chem. Soc.* **2009**, *131*, 6050–6051.
- (2) Lee, M. M.; Teuscher, J.; Miyasaka, T.; Murakami, T. N.; Snaith, H. J. Efficient Hybrid Solar Cells Based on Meso-Superstructured Organometal Halide Perovskites. *Science* **2012**, *338*, 643–647.
- (3) Burschka, J.; Pellet, N.; Moon, S.-J.; Humphry-Baker, R.; Gao, P.; Nazeeruddin, M. K.; Grätzel, M. Sequential Deposition as a Route to High-Performance Perovskite-Sensitized Solar Cells. *Nature* **2013**, *499*, 316–319.
- (4) Zhou, H.; Chen, Q.; Li, G.; Luo, S.; Song, T.-b.; Duan, H.-S.; Hong, Z.; You, J.; Liu, Y.; Yang, Y. Interface Engineering of Highly Efficient Perovskite Solar Cells. *Science* **2014**, *345*, 542–546.
- (5) Jeon, N. J.; Noh, J. H.; Yang, W. S.; Kim, Y. C.; Ryu, S.; Seo, J.; Seok, S. I. Compositional Engineering of Perovskite Materials for High-Performance Solar Cells. *Nature* **2015**, *517*, 476–480.
- (6) Research Cell Efficiency Records. National Renewable Energy Laboratory, 2016. <http://www.nrel.gov/ncp> (accessed Apr 1, 2016).
- (7) Zhao, Y.; Zhu, K. Organic–Inorganic Hybrid Lead Halide Perovskites for Optoelectronic and Electronic Applications. *Chem. Soc. Rev.* **2016**, *45*, 655–689.
- (8) Chin, X. Y.; Cortecchia, D.; Yin, J.; Bruno, A.; Soci, C. Lead Iodide Perovskite Light-Emitting Field-Effect Transistor. *Nat. Commun.* **2015**, *6*, No. 7383.
- (9) Mei, Y.; Zhang, C.; Vardeny, Z. V.; Jurchescu, O. D. Electrostatic Gating of Hybrid Halide Perovskite Field-Effect Transistors: Balanced Ambipolar Transport at Room-Temperature. *MRS Commun.* **2015**, *5*, 297–301.
- (10) Tan, Z.-K.; Moghaddam, R. S.; Lai, M. L.; Docampo, P.; Higler, R.; Deschler, F.; Price, M.; Sadhanala, A.; Pazos, L. M.; Credgington, D.; Hanusch, F.; Bein, T.; Snaith, H. J.; Friend, R. H. Bright Light-Emitting Diodes Based on Organometal Halide Perovskite. *Nat. Nanotechnol.* **2014**, *9*, 687–692.
- (11) Cho, H.; Jeong, S.-H.; Park, M.-H.; Kim, Y.-H.; Wolf, C.; Lee, C.-L.; Heo, J. H.; Sadhanala, A.; Myoung, N.; Yoo, S.; Im, S. H.; Friend, R. H.; Lee, T.-W. Overcoming the Electroluminescence Efficiency Limitations of Perovskite Light-Emitting Diodes. *Science* **2015**, *350*, 1222–1225.
- (12) Wong, A. B.; Lai, M.; Eaton, S. W.; Yu, Y.; Lin, E.; Dou, L.; Fu, A.; Yang, P. Growth and Anion Exchange Conversion of CH₃NH₃PbX₃ Nanorod Arrays for Light-Emitting Diodes. *Nano Lett.* **2015**, *15*, 5519–5524.

- (13) Wang, F.; Mei, J.; Wang, Y.; Zhang, L.; Zhao, H.; Zhao, D. Fast Photoconductive Responses in Organometal Halide Perovskite Photodetectors. *ACS Appl. Mater. Interfaces* **2016**, *8*, 2840–2846.
- (14) Ramasamy, P.; Lim, D.-H.; Kim, B.; Lee, S.-H.; Lee, M.-S.; Lee, J.-S. All-Inorganic Cesium Lead Halide Perovskite Nanocrystals for Photodetector Applications. *Chem. Commun.* **2016**, *52*, 2067–2070.
- (15) Zhang, F.; Zhong, H.; Chen, C.; Wu, X.-g.; Hu, X.; Huang, H.; Han, J.; Zou, B.; Dong, Y. Brightly Luminescent and Color-Tunable Colloidal $\text{CH}_3\text{NH}_3\text{PbX}_3$ (X = Br, I, Cl) Quantum Dots: Potential Alternatives for Display Technology. *ACS Nano* **2015**, *9*, 4533–4542.
- (16) Dou, L.; Wong, A. B.; Yu, Y.; Lai, M.; Kornienko, N.; Eaton, S. W.; Fu, A.; Bischak, C. G.; Ma, J.; Ding, T.; Ginsberg, N. S.; Wang, L.-W.; Alivisatos, A. P.; Yang, P. Atomically Thin Two-Dimensional Organic-Inorganic Hybrid Perovskites. *Science* **2015**, *349*, 1518–1521.
- (17) Saidaminov, M. L.; Adinolfi, V.; Comin, R.; Abdelhady, A. L.; Peng, W.; Dursun, I.; Yuan, M.; Hoogland, S.; Sargent, E. H.; Bakr, O. M. Planar-Integrated Single-Crystalline Perovskite Photodetectors. *Nat. Commun.* **2015**, *6*, No. 8724.
- (18) Zhu, H.; Fu, Y.; Meng, F.; Wu, X.; Gong, Z.; Ding, Q.; Gustafsson, M. V.; Trinh, M. T.; Jin, S.; Zhu, X.-Y. Lead Halide Perovskite Nanowire Lasers with Low Lasing Thresholds and High Quality Factors. *Nat. Mater.* **2015**, *14*, 636–642.
- (19) Fu, Y.; Zhu, H.; Schrader, A. W.; Liang, D.; Ding, Q.; Joshi, P.; Hwang, L.; Zhu, X.-Y.; Jin, S. Nanowire Lasers of Formamidinium Lead Halide Perovskites and Their Stabilized Alloys with Improved Stability. *Nano Lett.* **2016**, *16*, 1000–1008.
- (20) Xing, J.; Liu, X. F.; Zhang, Q.; Ha, S. T.; Yuan, Y. W.; Shen, C.; Sum, T. C.; Xiong, Q. Vapor Phase Synthesis of Organometal Halide Perovskite Nanowires for Tunable Room-Temperature Nanolasers. *Nano Lett.* **2015**, *15*, 4571–4577.
- (21) Eaton, S. W.; Lai, M.; Gibson, N. A.; Wong, A. B.; Dou, L.; Ma, J.; Wang, L.-W.; Leone, S. R.; Yang, P. Lasing in Robust Cesium Lead Halide Perovskite Nanowires. *Proc. Natl. Acad. Sci. U.S.A.* **2016**, *113*, 1993–1998.
- (22) Tian, W.; Zhao, C.; Leng, J.; Cui, R.; Jin, S. Visualizing Carrier Diffusion in Individual Single-Crystal Organolead Halide Perovskite Nanowires and Nanoplates. *J. Am. Chem. Soc.* **2015**, *137*, 12458–12461.
- (23) Li, Y. J.; Lv, Y.; Zou, C.-L.; Zhang, W.; Yao, J.; Zhao, Y. S. Output Coupling of Perovskite Lasers from Embedded Nanoscale Plasmonic Waveguides. *J. Am. Chem. Soc.* **2016**, *138*, 2122–2125.
- (24) Saxena, D.; Mokkaapati, S.; Parkinson, P.; Jiang, N.; Gao, Q.; Tan, H. H.; Jagadish, C. Optically Pumped Room-Temperature GaAs Nanowire Lasers. *Nat. Photonics* **2013**, *7*, 963–968.
- (25) Huang, M. H.; Mao, S.; Feick, H.; Yan, H.; Wu, Y.; Kind, H.; Weber, E.; Russo, R.; Yang, P. Room-Temperature Ultraviolet Nanowire Nanolasers. *Science* **2001**, *292*, 1897–1899.
- (26) Liao, Q.; Hu, K.; Zhang, H.; Wang, X.; Yao, J.; Fu, H. Perovskite Microdisk Microlasers Self-Assembled from Solution. *Adv. Mater.* **2015**, *27*, 3405–3410.
- (27) Zhang, Q.; Ha, S. T.; Liu, X.; Sum, T. C.; Xiong, Q. Room-Temperature Near-Infrared High-Q Perovskite Whispering-Gallery Planar Nanolasers. *Nano Lett.* **2014**, *14*, 5995–6001.
- (28) Sutherland, B. R.; Hoogland, S.; Adachi, M. M.; Wong, C. T. O.; Sargent, E. H. Conformal Organohalide Perovskites Enable Lasing on Spherical Resonators. *ACS Nano* **2014**, *8*, 10947–10952.
- (29) Li, W.; Coppens, Z. J.; Besteiro, L. V.; Wang, W.; Govorov, A. O.; Valentine, J. Circularly Polarized Light Detection with Hot Electrons in Chiral Plasmonic Metamaterials. *Nat. Commun.* **2015**, *6*, No. 8379.
- (30) Wang, H.; Zhang, C.; Chan, W.; Tiwari, S.; Rana, F. Ultrafast Response of Monolayer Molybdenum Disulfide Photodetectors. *Nat. Commun.* **2015**, *6*, No. 8831.
- (31) Jansen-van Vuuren, R. D.; Armin, A.; Pandey, A. K.; Burn, P. L.; Meredith, P. Organic Photodiodes: The Future of Full Color Detection and Image Sensing. *Adv. Mater.* **2016**, *28*, 4766–4802.
- (32) Hu, X.; Zhang, X.; Liang, L.; Bao, J.; Li, S.; Yang, W.; Xie, Y. High-Performance Flexible Broadband Photodetector Based on Organolead Halide Perovskite. *Adv. Funct. Mater.* **2014**, *24*, 7373–7380.
- (33) Dou, L.; Yang, Y. M.; You, J.; Hong, Z.; Chang, W.-H.; Li, G.; Yang, Y. Solution-Processed Hybrid Perovskite Photodetectors with High Detectivity. *Nat. Commun.* **2014**, *5*, No. 5404.
- (34) Zhang, D.; Eaton, S. W.; Yu, Y.; Dou, L.; Yang, P. Solution-Phase Synthesis of Cesium Lead Halide Perovskite Nanowires. *J. Am. Chem. Soc.* **2015**, *137*, 9230–9233.
- (35) Wang, Z.; Liu, J.; Xu, Z.-Q.; Xue, Y.; Jiang, L.; Song, J.; Huang, F.; Wang, Y.; Zhong, Y. L.; Zhang, Y.; Cheng, Y.-B.; Bao, Q. Wavelength-Tunable Waveguides Based on Polycrystalline Organic-Inorganic Perovskite Microwires. *Nanoscale* **2016**, *8*, 6258–6264.
- (36) Mei, A.; Li, X.; Liu, L.; Ku, Z.; Liu, T.; Rong, Y.; Xu, M.; Hu, M.; Chen, J.; Yang, Y.; Gratzel, M.; Han, H. A Hole-Conductor-Free, Fully Printable Mesoscopic Perovskite Solar Cell with High Stability. *Science* **2014**, *345*, 295–298.
- (37) Chen, Q.; Zhou, H.; Song, T.-B.; Luo, S.; Hong, Z.; Duan, H.-S.; Dou, L.; Liu, Y.; Yang, Y. Controllable Self-Induced Passivation of Hybrid Lead Iodide Perovskites toward High Performance Solar Cells. *Nano Lett.* **2014**, *14*, 4158–4163.
- (38) Yang, W. S.; Noh, J. H.; Jeon, N. J.; Kim, Y. C.; Ryu, S.; Seo, J.; Seok, S. I. High-Performance Photovoltaic Perovskite Layers Fabricated through Intramolecular Exchange. *Science* **2015**, *348*, 1234–1237.
- (39) Han, Q.; Bae, S.-H.; Sun, P.; Hsieh, Y.-T.; Yang, Y. M.; Rim, Y. S.; Zhao, H.; Chen, Q.; Shi, W.; Li, G.; Yang, Y. Single Crystal Formamidinium Lead Iodide (FAPbI₃): Insight into the Structural, Optical, and Electrical Properties. *Adv. Mater.* **2016**, *28*, 2253–2258.
- (40) Eperon, G. E.; Stranks, S. D.; Menelaou, C.; Johnston, M. B.; Herz, L. M.; Snaith, H. J. Formamidinium Lead Trihalide: a Broadly Tunable Perovskite for Efficient Planar Heterojunction Solar Cells. *Energy Environ. Sci.* **2014**, *7*, 982.
- (41) Lee, S. J.; Shin, S. S.; Kim, Y. C.; Kim, D.; Ahn, T. K.; Noh, J. H.; Seo, J.; Seok, S. I. Fabrication of Efficient Formamidinium Tin Iodide Perovskite Solar Cells through SnF-Pyrazine Complex. *J. Am. Chem. Soc.* **2016**, *138*, 3974–3977.
- (42) Ito, S.; Tanaka, S.; Manabe, K.; Nishino, H. Effects of Surface Blocking Layer of Sb₂S₃ on Nanocrystalline TiO₂ for CH₃NH₃PbI₃ Perovskite Solar Cells. *J. Phys. Chem. C* **2014**, *118*, 16995–17000.
- (43) Tan, H.; Jain, A.; Voznyy, O.; Lan, X.; de Arquer, F. P. G.; Fan, J. Z.; Quintero-Bermudez, R.; Yuan, M.; Zhang, B.; Zhao, Y.; Fan, F.; Li, P.; Quan, L. N.; Zhao, Y.; Lu, Z. H.; Yang, Z.; Hoogland, S.; Sargent, E. H. Efficient and Stable Solution-Processed Planar Perovskite Solar Cells via Contact Passivation. *Science* **2017**, *355*, 722–726.
- (44) Saliba, M.; Matsui, T.; Domanski, K.; Seo, J.-Y.; Ummadisingu, A.; Zakeeruddin, S. M.; Correa-Baena, J.-P.; Tress, W. R.; Abate, A.; Hagfeldt, A.; Gratzel, M. Incorporation of Rubidium Cations into Perovskite Solar Cells Improves Photovoltaic Performance. *Science* **2016**, *354*, 206–209.
- (45) Protesescu, L.; Yakunin, S.; Kumar, S.; Bär, J.; Bertolotti, F.; Masciocchi, N.; Guagliardi, A.; Grotevent, M.; Shorubalko, I.; Bodnarchuk, M. I.; Shih, C.-J.; Kovalenko, M. V. Dismantling the “Red Wall” of Colloidal Perovskites: Highly Luminescent Formamidinium and Formamidinium–Cesium Lead Iodide Nanocrystals. *ACS Nano* **2017**, *11*, 3119–3134.
- (46) Stoumpos, C. C.; Malliakas, C. D.; Kanatzidis, M. G. Semiconducting Tin and Lead Iodide Perovskites with Organic Cations: Phase Transitions, High Mobilities, and Near-Infrared Photoluminescent Properties. *Inorg. Chem.* **2013**, *52*, 9019–9038.
- (47) Eperon, G. E.; Paternò, G. M.; Sutton, R. J.; Zampetti, A.; Haghighirad, A. A.; Cacialli, F.; Snaith, H. J. Inorganic Cesium Lead Iodide Perovskite Solar Cells. *J. Mater. Chem. A* **2015**, *3*, 19688–19695.
- (48) Shen, D.; Yu, X.; Cai, X.; Peng, M.; Ma, Y.; Su, X.; Xiao, L.; Zou, D. Understanding the Solvent-Assisted Crystallization Mechanism Inherent in Efficient Organic–inorganic Halide Perovskite Solar Cells. *J. Mater. Chem. A* **2014**, *2*, 20454–20461.

(49) Fu, F.; Kranz, L.; Yoon, S.; Löckinger, J.; Jäger, T.; Perrenoud, J.; Feurer, T.; Gretener, C.; Buecheler, S.; Tiwari, A. N. Controlled Growth of PbI_2 Nanoplates for rapid Preparation of $\text{CH}_3\text{NH}_3\text{PbI}_3$ in Planar Perovskite Solar Cells. *Phys. Status Solidi A* **2015**, *212*, 2708–2717.

(50) Wang, F.; Yu, H.; Xu, H.; Zhao, N. HPbI_3 : A New Precursor Compound for Highly Efficient Solution-Processed Perovskite Solar Cells. *Adv. Funct. Mater.* **2015**, *25*, 1120–1126.

(51) Jung, H. S.; Park, N.-G. Perovskite Solar Cells: from Materials to Devices. *Small* **2015**, *11*, 10–25.

(52) Wang, F.-X.; Lin, J.; Gu, W.-B.; Liu, Y.-Q.; Wu, H.-D.; Pan, G.-B. Aerosol-jet Printing of Nanowire Networks of Zinc Octaethylporphyrin and its Application in Flexible Photodetectors. *Chem. Commun.* **2013**, *49*, 2433–2435.

(53) Chen, G.; Liu, Z.; Liang, B.; Yu, G.; Xie, Z.; Huang, H.; Liu, B.; Wang, X.; Chen, D.; Zhu, M.-Q.; Shen, G. Single-Crystalline p-Type Zn_3As_2 Nanowires for Field-Effect Transistors and Visible-Light Photodetectors on Rigid and Flexible Substrates. *Adv. Funct. Mater.* **2013**, *23*, 2681–2690.